Journal of Materials Chemistry B

PAPER

View Article Online
View Journal | View Issue

Cite this: J. Mater. Chem. B, 2017, 5, 4152

NIR-driven water splitting by layered bismuth oxyhalide sheets for effective photodynamic therapy†

Dan Yang, Guixin Yang, Jiaqi Li, Shili Gai,* Fei He* and Piaoping Yang*

Received 13th March 2017,
Accepted 8th May 2017

DOI: 10.1039/c7tb00688h

rsc.li/materials-b

Two major issues of finding the appropriate photosensitizer and raising the penetration depth of irradiation light exist in further developing of photodynamic therapy (PDT). The excited ultraviolet/visible (UV/vis) irradiation light has a relatively shallow depth of penetration and UV light itself may have sufficient energy to damage normal tissues; these are substantial limitations to successful cancer therapy. Herein, we for the first time report a novel multifunctional nanoplatform for a single 980 nm near-infrared (NIR) light-triggered PDT based on $NaGdF_4$:Yb,Tm@$NaGdF_4$ upconversion nanoparticles (UCNPs) integrated with bismuth oxyhalide (BiOCl) sheets, designated as UCNPs@BiOCl. And UCNPs@BiOCl was fabricated by a convenient, efficient, green, and inexpensive method. Excitingly, layered bismuth oxyhalide materials possess a high photocatalytic performance, unique layered structures and wide light response to a broad wavelength range of ultraviolet to visible light. And the loaded UCNPs can convert NIR light into UV/vis region emissions, which drives the pure water splitting of BiOCl sheets to produce plenty of reactive oxygen species (ROS) to damage tumor cells. The excellent antitumor efficiency of the complex has been evidently attested by comparing experimental results. Our work may make a contribution to the wide application of BiOCl-based materials in biomedicine.

Introduction

Photodynamic therapy (PDT), with fewer side effects, more remarkable cell selectivity and lower systematic toxicity compared to conventional radiotherapeutic and chemotherapeutic methods, has been proposed as a minimally invasive surgical technology and clinically used in the biomedicine field.[1–6] As is known, three essential ingredients in PDT are the photosensitizer, reactive oxygen species (ROS), and irradiation light.[7–10] Many researchers have devoted efforts to find a proper photosensitizer and to increase the penetration depth of irradiation light in PDT.[11–14] In general, the high abilities of oxidation and photocatalytic reduction are entrusted to traditional photosensitizers for the wide band gap. Unfortunately, they only can be excited by ultraviolet/visible light, which has a low tissue penetration that limits successful cancer therapy. To increase the penetration depth, many attempts have been dedicated and new PDT systems were developed to overcome this drawback.[15–19]

Recently, photocatalytic materials, such as carbon nitride materials,[20–23] TiO_2[24–26] and ZnO,[27–31] have acquired more and more attention as they are fundamentally and technologically intriguing for plentiful and promising applications in biomedicine, electronics, energy storage and catalysis. Especially, efficiently photocatalysts have been diffusely applied in PDT as inorganic photosensitizers, which is attributed to light-induced water splitting followed by producing reactive oxygen species (ROS) to damage cancer cells.[32–36] Particularly, layered bismuth oxyhalide materials are developed as promising inorganic photosensitizers in tumor PDT due to their high photocatalytic performance, unique layered structures and wide light response to a broad wavelength range from ultraviolet to visible light. Bismuth oxy-halide BiOCl, as an alternative photosensitizer, belongs to a new class of potentially layered semiconductors with an adjustable band gap through controlling the structure, and fascinating physicochemical properties based on a unique layered structure.[37–39] The layered structures are [Cl–Bi–O–Bi–Cl] slices stacked together by the weak interlayer van der Waals interaction giving rise to BiOCl with many excellent properties, involving highly optical, electrical, and mechanical properties.[40–43] So, BiOCl possesses potential applications in water splitting, photocatalytic waste water and indoor-gas purification, selective oxidation of alcohols and organic synthesis.[40,44] In the past five years, many scientific workers have reported plenty of exciting contributions to improve the

Key Laboratory of Superlight Materials and Surface Technology, Ministry of Education, College of Material Sciences and Chemical Engineering, Harbin Engineering University, Harbin, 150001, P. R. China.
E-mail: yangpiaoping@hrbeu.edu.cn, gaishili@hrbeu.edu.cn, hefei1@hrbeu.edu.cn

† Electronic supplementary information (ESI) available. See DOI: 10.1039/c7tb00688h

visible-light-driven photocatalytic activity of BiOCl,[45,46] such as, an optimum synthesis of 2D BiOX (X = Cl, Br and I) nanosheets, co-catalyst utilization, modification of BiOX, photocatalyst coupling, surface plasmon resonance, and element doping.[47–50] However, the application of bismuth oxyhalides in PDT has rarely been reported. Furthermore, the UV or visible irradiation light used has a relatively shallow penetration depth and UV light with sufficient energy may damage normal tissues, which may greatly limit their therapeutic application in PDT. Thus, the combination of bismuth oxyhalides with up-conversion nanoparticles (UCNPs) which can convert the high-penetrating NIR to UV/visible light is a feasible route to solve the above-mentioned problems.

As is known, up-conversion luminescence (UCL) materials could convert low energy light, usually NIR, to higher energy light (UV or vis light) *via* the fluorescence resonance energy transfer (FRET) process, and they have been widely proposed for use in many fields, including anticancer therapy, bioimaging, and photovoltaic technologies.[51–55] Moreover, the absence of background fluorescence and the deep tissue penetration in a biological environment under laser excitation are the two remarkable characters of rare-earth UCNPs as luminescent probes in biological imaging and labeling technology.[56–58] Compared with quantum dots, semiconductor and organic fluorophores, some rare-earth UCNPs under a continuous-wave (CW) NIR excitation present unique UCL properties, such as a high photostability, large anti-Stokes shift and sharp emission lines that depend on the f–f transition.[59–70]

Herein, we, for the first time, propose an UCNPs@BiOCl nanoplatform for high-efficiency PDT induced by NIR light with a convenient, efficient, green, and inexpensive method. The UCL materials could convert the NIR irradiation to UV or vis light *via* an upconversion energy transfer process, thus mediating the photosensitizer (BiOCl) to produce ROS. Meanwhile, it is known that extensive tissue penetration is propitious to enhance the light absorption of a drug carrier and the light-driven PDT effect. Thus, modifying BiOCl sheets with UCNPs is a suitable way to design a multifunctional composite. In this way, the combination of UCNPs has solved both visible-light-driven photocatalytic activity and tissue penetration in the anticancer therapy and nanomedicine fields, and UCNPs can also provide support for imaging-guided tumor PDT. Importantly, the photodynamic effect of UCNPs@BiOCl is more prominent than similar state-of-the-art materials, owing to the high photocatalytic performance of BiOCl sheets.

Results and discussion

Synthesis and characterization of the samples

Scheme 1 shows the construction of UCNPs@BiOCl. It integrates PAA modified UCNPs with PEI modified BiOCl. The UCNPs could convert NIR light (980 nm) to UV and visible lights (blue and red emission) *via* multiple-photon process. BiOCl nanosheets can absorb both the emitted UV and visible lights to further generate ROS, and also the emitted blue light can be used for UCL imaging diagnosis. Thus, through the

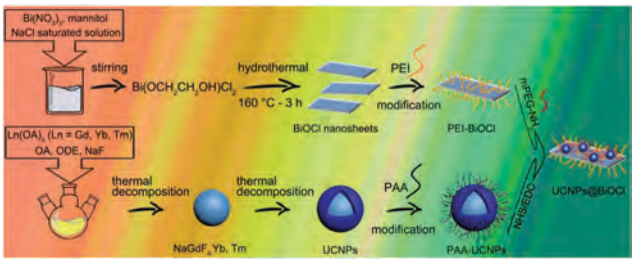

Scheme 1 Schematic illustration for the formation of the UCNPs@BiOCl composite.

incorporation of the two counterparts, the UCNPs@BiOCl excited with 980 nm light can be employed for image guided PDT.

As the 980 nm light-triggered component of the whole therapy system, the core/shell structured $NaGdF_4$:Yb,Tm@$NaGdF_4$ is prepared through a successive layer-by-layer strategy using oleic acid as the stabilizing agent, which was reported by us previously. To achieve a better UC emission for a more excellent imaging diagnosis and PDT, we designed the two-layer core/shell $NaGdF_4$:Yb,Tm@$NaGdF_4$ structure (Fig. 1B). Transmission electron microscopy (TEM) characterization shows a monodispersed particle size of the core $NaGdF_4$:Yb,Tm (~32 nm) and the core/shell UCNPs (~36 nm) (Fig. 1A and B). Meanwhile, a differentiable increase of the particle size is found with the coated layer, and the shape and average size of the two-layer UCNPs (Fig. 1B) can be well maintained at 36 nm. As expected, compared with the $NaGdF_4$:Yb,Tm core, the UCL emission intensity of UCNPs has been dramatically advanced because of the quenching-shield $NaGdF_4$ shell (Fig. 1D). The emissions at 338, 360, 440–480, and 650–670 nm of UCNPs under 980 nm laser excitation are assigned to the $^1I_6 \rightarrow {}^3F_4$, $^1D_2/^1G_4/^3F_2 \rightarrow {}^3H_6$, and $^1D_2 \rightarrow {}^3F_4$ transitions of Tm^{3+} ions, respectively. Meanwhile, the highly crystalline and hexagonal phase of the UCNPs have been confirmed by powder X-ray diffraction (Fig. S1, ESI†).

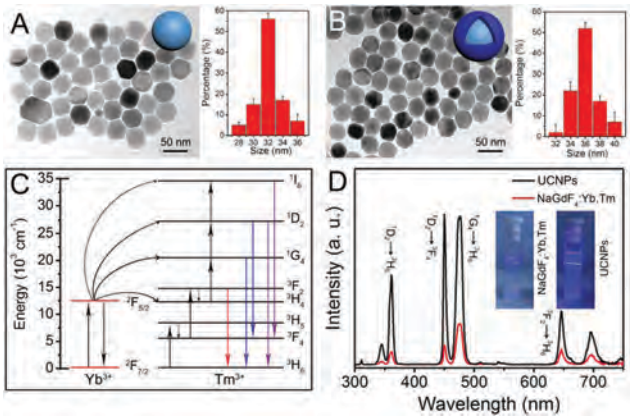

Fig. 1 (A) TEM images of $NaGdF_4$:Yb,Tm. (B) TEM images of UCNPs. Insets are the corresponding particle size distribution and model. (C) Proposed energy-transfer mechanism of Yb and Tm doped nanoparticles upon 980 nm laser excitation. (D) UC emission spectra of $NaGdF_4$:Yb,Tm and UCNPs under 980 nm laser excitation. Insets are the photographs of $NaGdF_4$:Yb,Tm (left) and UCNP (right) particles under 980 nm irradiation.

To assemble the UCNPs on the BiOCl nanosheets, the oleic acid (OA)-capped UCNPs in an oil phase were transferred to the aqueous phase through a ligand exchange reaction with PAA. FT-IR spectroscopy was used to verify the functionalization of PAA on the UCNPs, and the corresponding spectra of PAA–UCNPs, PEI–BiOCl, and UCNPs@BiOCl are presented in Fig. S2 (ESI†). As shown, a similar band is displayed in all four samples at 3457 cm^{-1} for –OH stretching. Two strong bands centered at around 1563 cm^{-1} and 1457 cm^{-1} are found for OA–UCNPs, which are ascribed to the symmetric and asymmetric vibration modes of carboxylate anions on the surface of the UCNPs. Compared with oleic acid coated UCNPs, the strong characteristic absorption band centered at around 1732 cm^{-1} in PAA–UCNPs indicates an increased quantity of the carboxyl groups on the UCNP surfaces and the successful linkage of PAA.

As the photosensitizer plays the key role in the whole therapy system, the well-defined square-like structured BiOCl nanosheets are synthesized according to the synthesis method reported by Chen *et al.*[43] As seen in the X-ray powder diffraction (XRD) pattern of BiOCl nanosheets (Fig. S1, ESI†), the diffraction peaks of the sample can be easily indexed to the reference data (JCPS card No. 06-249) of an exactly tetragonal matlockite BiOCl phase. The microstructures and morphologies of the BiOCl nanosheets are characterized by TEM observations. It is clearly seen that the average size of all the BiOCl particles is in the shape of nanosheets with a well-defined dispersal and all of them will be maintained further in a biomedical field. The atomic force microscopy (AFM) image of BiOCl nanosheets and their height profiles along the black lines are shown in Fig. 2B and C. As shown, all the heights of the BiOCl nanosheets are nano-sized. The BiOCl nanosheets are broken and modified using PEI for further conjunction with UCNPs, and the corresponding Fourier transform infrared (FT-IR) spectra of PEI–BiOCl are also presented in Fig. S2 (ESI†). As shown, the characteristic absorption bands of N–H (3434 cm^{-1}) and, N–H (1653 cm^{-1}) are the stretch and deformation vibration modes of the N–H bond in the $–NH_2–$ group in PEI–BiOCl, suggesting the successful functionalization of PEI.

Fig. 3 shows the TEM images of the UCNPs@BiOCl complex. As shown, the smaller UCNPs are distributed on the surface of BiOCl nanosheets. After linkage of the PAA–UCNPs, two parts of the crystal lattices can be found in the XRD pattern of the UCNPs@BiOCl complex (Fig. S1, ESI†). X-ray photoelectron spectrum (XPS) is employed to further confirm the surface elements of the UCNPs@BiOCl complex, including Na, Gd, Yb, Tm, Bi, C, O, F, and Cl (Fig. 3C), which is also verified by the results of statistical EDS analysis given in Fig. 3D.

After functionalization with BiOCl, the UCL properties of the UCNPs have an appreciable drop in the whole emission region. Fig. 4 shows the UCL characteristics of UCNPs and UCNPs@BiOCl; all the samples were exposed in same laser power density (0.5 W cm^{-2}). The red emission at 650 nm in the fluorescence spectrum of UCNPs@BiOCl almost disappears, suggesting an efficient energy transfer from UCNPs to BiOCl caused by the sequential absorption of multiple photons. Fig. 4C and D show the decay curves at 475 nm ($^1G_4 \rightarrow {}^3H_6$ transition) and

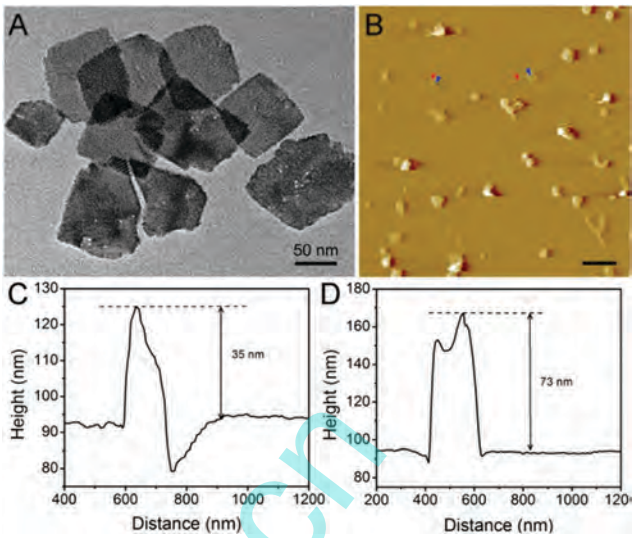

Fig. 2 (A) TEM image of BiOCl nanosheets. (B) AFM image of BiOCl sheets and height profiles along the two black lines (C and D). Scale bar in panel B is 500 nm.

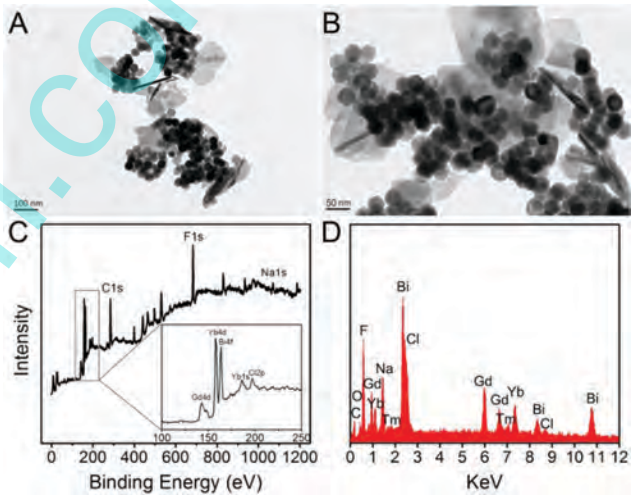

Fig. 3 (A) Low- and (B) high-magnified TEM images of UCNPs@BiOCl. XPS (C) and EDS (D) of UCNPs@BiOCl composite.

650 nm ($^3F_2 \rightarrow {}^3H_6$ transition) of the UCNPs and UCNPs@BiOCl under NIR light excitation. The lifetimes of the two samples decrease from 0.94 to 0.77 ms and from 0.89 to 0.68 ms, respectively, further proving the FRET process. Excitingly, the strong blue light emissions still exist in the UCNPs@BiOCl under NIR light irradiation, indicating its possible use for UCL imaging to diagnose a tumor location or track the carrier position (Fig. 4B). As shown in Fig. 4E, under NIR light irradiation, the cells taken up in the complex can emit bright blue light, and the evidently intracellular UCL signals are found.

Bio-stability in a stimulated body fluid (SBF)

If it is to be applied in the bio-medical field, the complex should be evaluated for the bio-stability in a SBF, such as fetal bovine serum and normal saline. The UCNPs@BiOCl complex

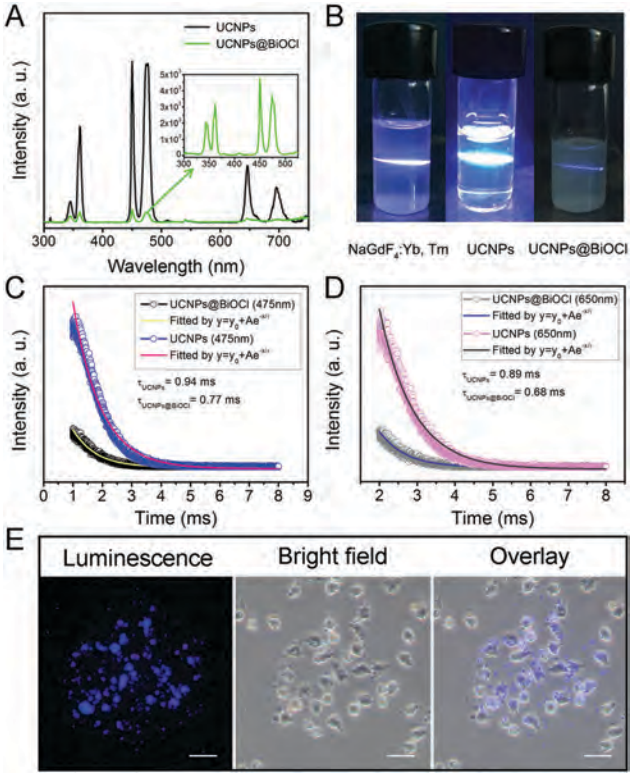

Fig. 4 Upconversion luminescence properties of UCNPs and UCNPs@BiOCl. (A) UCL spectra under 980 nm laser irradiation. (B) Photographs of $NaGdF_4$:Yb,Tm, UCNPs and UCNPs@BiOCl in a PBS solution under 980 nm irradiation. Decay curves at wavelengths of (C) 475 and (D) 650 nm. (E) *In vitro* UCL imaging properties. Inverted fluorescence microscope images of HeLa cells incubated with UCNPs@BiOCl for 3 h at 37 °C. Scale bars for all images are 25 μm.

is dispersed into the fetal bovine serum and normal saline, followed by mildly shaking at 37 °C. The digital photos of the two solutions and the corresponding absorbance spectra at particular points in time (0, 2, 5, 7, and 14 days) are recorded. As shown in Fig. 5, no difference appeared in the two sample solutions (insets, Fig. 5A and B). The absorbance intensity has a negligible decrease because of the inevitable error in the test. Moreover, the absorbance also exists in the whole visible region, which is consistent with the absorbance spectrum of BiOCl nanosheets. On day 14, the size distributions of UCNPs@BiOCl dispersed into the two solutions were confirmed by Dynamic Light Scattering (DLS). No substantial difference in size reveals that they almost maintain a good dispersion after 14 days of standing (Fig. S3A and B, ESI†). Fig. S4 (ESI†) shows that the zeta potential curves of the as-made UCNPs@BiOCl in the two media are −21.5 and −22.9 mV, respectively. All the above results reveal that the bio-stability of the complex in the normal saline and fetal bovine serum is good.

Extracellular and intracellular singlet oxygen detection

As presented in Fig. 6, the emission spectrum of UCNPs with 980 nm laser excitation is well matched with the absorption spectrum of BiOCl, implying a possible energy transfer. We were encouraged and decided to detect the photodynamic

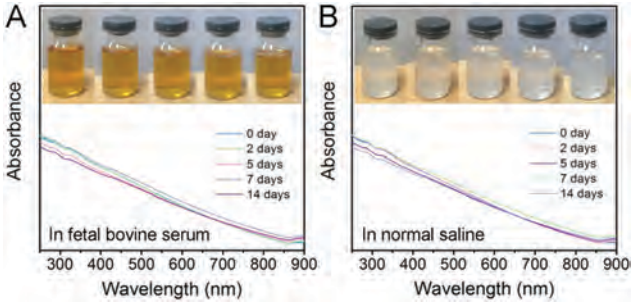

Fig. 5 Photographs and absorbance spectra of the UCNPs@BiOCl solutions in fetal bovine serum (A) and normal saline (B) after 14th days-standing.

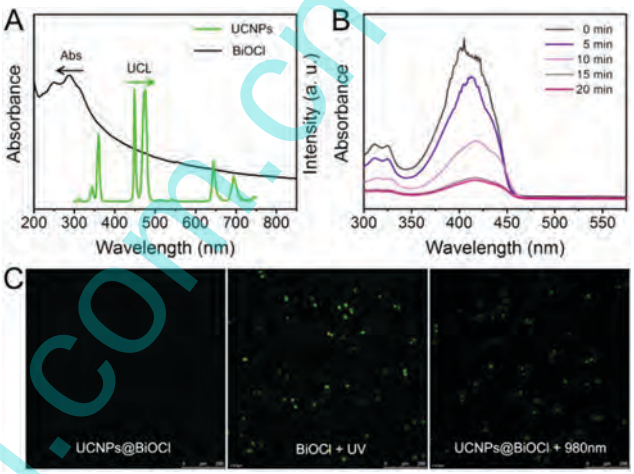

Fig. 6 (A) The emission spectrum of UCNPs under 980 nm laser excitation and the absorption spectrum of BiOCl photosensitizer. (B) Time-course absorbance spectrum of DPBF mixed with UCNPs@BiOCl at a wavelength of 410 nm under a 980 nm laser (0.5 W cm^{-2}). (C) CLSM images of HeLa cells incubated with UCNPs@BiOCl, BiOCl under UV light irradiation, and UCNPs@BiOCl under 980 nm laser irradiation. All the cells were marked with DCFH-DA.

properties of the complex, Here, to verify the photodynamic properties of the complex in the solution, DPBF was employed as the ROS probe. And DCFH-DA was utilized for the measurement *in vitro*. In the presence of ROS, DPBF is degraded, giving rise to a decrease in the absorbance intensity at a wavelength of 410 nm. As shown in Fig. 6B, the absorbance intensities are inordinately decreased with a prolonged irradiation time. The photodynamic properties of the complex are detected using DCFH-DA to assess the intracellular ROS. After DCFH-DA is taken up by cells and hydrolysis to DCFH by the intracellular esterase, the DCF molecules oxidized from DCFH are attributed to the presence of intracellular ROS. In this process, only DCF can emit a strong green fluorescence (λ_{em} = 525 nm) at an irradiation wavelength of 488 nm. The confocal laser scanning microscopy (CLSM) images of HeLa cells with oxidized DCF fluorescence are shown in Fig. 6C and Fig. S5 (ESI†). From marking with the green luminescence, the ROS generating capability of BiOCl under UV light irradiation and of UCNPs@BiOCl under 980 nm light irradiation is similar. Additionally, the quantitative comparison of the singlet oxygen production efficacy of UCNPs@BiOCl excited

by 980 nm and UV are provided in Fig. S6 (ESI†). The results indicated that the absorbance intensity of DPBF6 mixed with UCNPs@BiOCl and excited by UV is slightly lower than the group mixed with UCNPs@BiOCl and excited by 980 nm. The results indicated that the use of 980 nm light and UCNPs replaces the normal UV/vis light to produce ROS, which is very important to raise the tissue penetration of the excitation light in therapy application.

Moreover, the photodynamic properties of the complex are directly compared with similar state-of-the-art materials consisting of a photosensitizer in combination with UCNPs for photodynamic therapy. The results are shown in Fig. S7 (ESI†). In the group mixed with UCNPs@BiOCl, the absorbance intensity at a wavelength of 410 nm is likely to decline by more than 80% upon intermittent illumination in 24 h. The relatively weaker decline present in the other comparing groups indicates the higher efficiency photodynamic effect of UCNPs@BiOCl.

Biocompatibility and hemolysis properties

Before the complexes were taken on as potential theranostic agents, it was also essential to evaluate the biocompatibility and hemolysis. Firstly, cell viability was estimated with L929 mouse fibroblast cells by a conventional 3-(4,5-dimethylthiazol-2-yl)-2,5-diphenyltetrazolium bromide (MTT) assay. The cytotoxicity was recorded after incubation for 24 h with 0.1 mL of different concentrations of the UCNPs@BiOCl complex (Experimental section). The data are average calculated by three parallel groups, and according to the following equation: cell survival (%) = $OD_{treatment\ group}/OD_{control\ group} \times 100\%$. The complex shows almost no dark cytotoxicity to the L929 cells with concentrations from 7.8 to 500 μg mL^{-1} (Fig. 7A). The results indicate that the prepared UCNPs@BiOCl have a very low toxicity, making it suitable for utilization as a drug nanocarrier. Moreover, to investigate the hemolysis of UCNPs@BiOCl, the complex was cultured with human red blood cells. The mixture of 1.2 mL of PBS and 0.3 mL of diluted RBCs is the negative control group, and 1.2 mL of deionized water was mixed with 0.3 mL of diluted RBCs, which served as a positive control group. From the results shown in Fig. 7B, hemoglobin separated from the red blood cells in the water will result in a red color of the tube (insets, Fig. 7B). By contrast, no visible red color is detected in the PBS solutions cultured with UCNPs@BiOCl even ay concentrations up to 500 μg mL^{-1}. 0.69% is the highest hemolytic value, suggesting hardly any hemolysis occurs. So, the complex can be employed for drug carriers, given the credit of a good compatibility of UCNPs@BiOCl with blood.

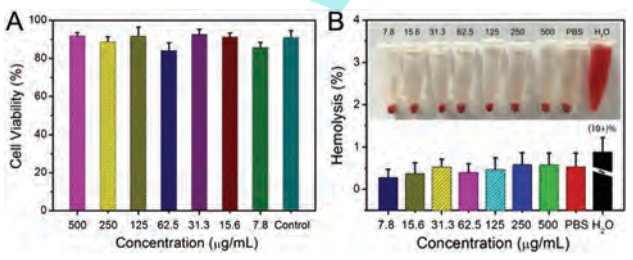

Fig. 7 (A) Cell viability for L929 cells incubated with 0.1 mL of UCNPs@BiOCl with different concentrations for 24 h. Cell viability was measured by MTT assay. (B) Hemolytic assay of UCNPs@BiOCl by human red blood cells. Data represents mean ± SD (n = 3).

MTT cytotoxicity assay *in vitro*

Encouraged by the photodynamic performance of NIR light-driven UCNPs@BiOCl shown in the solution, an MTT assay and dye experiment were further employed to evaluate the antitumor performances against HeLa cells *in vitro*. In Fig. 8A, the higher cell viability with a pure UCNPs@BiOCl complex treatment, which is not lower than the groups with cell-culture and pure laser irradiation, indicates that UCNPs@BiOCl are weakly toxic to cells. When samples are irradiated with NIR light, concentration-dependent cytotoxicity with cell viabilities of 28.9–11.6% are obtained, suggesting the highest anticancer efficiency of UCNPs@BiOCl complex with laser irradiation. The same conclusions can be vividly obtained from the dye experiment through identifying live/dead states of different treatment groups (Fig. 8B).

In vivo tumor inhibition effect

Further experiments were performed to investigate the antitumor efficacy of UCNPs@BiOCl *in vivo*. The tumor-bearing mice were divided into four groups (n = 5) randomly, and intravenously injected with normal saline as the control group. Treating with pure 980 nm irradiation, pure UCNPs@BiOCl and UCNPs@BiOCl with NIR light irradiation served as the treatment groups. The photos of representative mice with excised tumors after the initiation of the treatments with different conditions for 14 days are presented in Fig. 9C. It is confirmed that the tumor inhibition effect with UCNPs@BiOCl under NIR light irradiation shows the strongest, while pure UCNPs@BiOCl or NIR light barely has an inhibiting effect on the tumor size. Meanwhile, the body weights in all the groups presented sustained

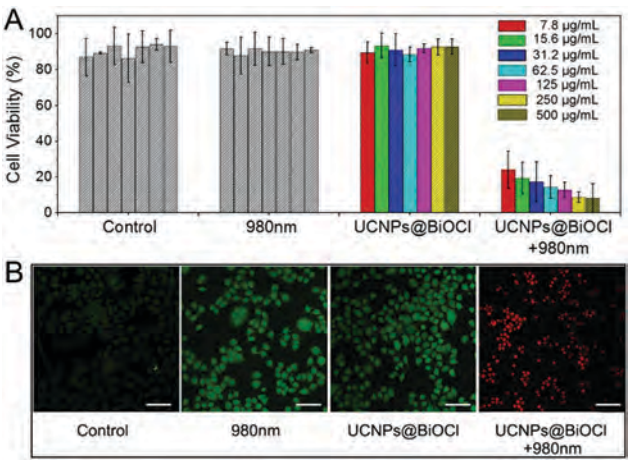

Fig. 8 (A) *In vitro* cell viabilities of HeLa cells incubated with cell-culture (control group), 980 nm light, pure UCNPs@BiOCl composites, and UCNPs@BiOCl with 980 nm laser irradiation at varied concentrations. (B) CLSM images of HeLa cells incubated with different conditions corresponding to the toxicity test *in vitro*, and all the cells are marked with calcein AM and PI. Scale bars for all the images are 100 μm.

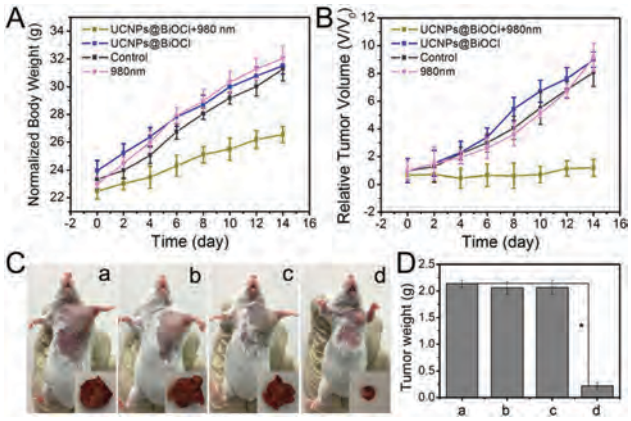

Fig. 9 *In vivo* anti-cancer properties. (A) The body weight and (B) relative tumor volume of tumor bearing mice in different groups *versus* the treatment time. (C) Representative photographs of tumor-bearing mice and tumor tissue excised from tumor-bearing mice treated with (a) normal saline, (b) pure UCNPs@BiOCl composite, (c) 980 nm, and (d) UCNPs@BiOCl with 980 nm laser irradiation on the 14th day. (D) The weight of tumor excised from tumor-bearing mice. $*p < 0.01$ *versus* control group. The data in the figures are average calculated for five mice per group.

growth and the survival rates are 100%, indicating a low toxicity of UCNPs@BiOCl (Fig. 9A). The results of the relative tumor volume (Fig. 9B) show that the tumor grew rapidly when treated with only NIR or the pure UCNPs@BiOCl complex, revealing the tumor growth is not affected by the NIR exposure or the pure UCNPs@BiOCl complex. However, the tumor growth inhibition effect of UCNPs@BiOCl with NIR irradiation is significant. Tumor sizes (Fig. 9C) and the corresponding H&E-stained images of the main tissues and organs (heart, spleen, kidney, liver, and lung) from different groups are shown in Fig. S8 (ESI†). In Fig. 9D, the results of the tumor show a positive inhibiting effect of UCNPs@BiOCl under NIR light irradiation, with only a bean size tumor-like feature after 14 days of treatment. Meanwhile, there were no abnormal phenomena in the H&E-stained images of each treatment group: no apparent damage and diseased region were observed in the examined organs and tissue from all the treatment groups, implying that the UCNPs@BiOCl complex has a good biocompatibility and inappreciable side effects.

The complete blood count assessment and serum biochemistry assay further indicate barely a potential toxicity of the UCNPs@BiOCl complex after 14 days of treatment. Complete blood counts, blood levels of hematocrit (HCT), hemoglobin (HGB), white blood cells (WBC), mean corpuscular hemoglobin (MCH), red blood cells (RBC), mean corpuscular volume (MCV), mean corpuscular hemoglobin concentration (MCHC), alanine aminotransferase (ALT), blood urea level (BUN), alkaline phosphatase (ALP), aspartate aminotransferase (AST), the ratio of albumin and globulin (A/G), and platelets (PLT) of healthy Balb/c mice and Balb/c mice treated with the UCNPs@BiOCl complex were recorded, and the statistics are based on 5 mice per data point (Table S1, ESI†). Compared with the healthy Balb/c mice, all the biochemistry results reveal that no clear signals of injury were found in kidney or liver and no obvious interference with the physiological regulation of the immune response for UCNPs@BiOCl particles. Therefore, these *in vitro* and *in vivo* results evidently demonstrate that the UCNPs@BiOCl complex is competent as a promising antitumor agent to provide great therapeutic efficacy under a single 980 nm irradiation.

Based on the Gd concentration in mouse blood at different times after the intravenous injection of the UCNPs@BiOCl nanoparticles, the drug eliminated half-life was calculated to be 4.68 h (Fig. S9, ESI†). From the curve of drug eliminated half-life, nanomaterial with a certain concentration still exists in the mouse blood, which can accumulate in the tumors of the mice and realize a sustained therapy. The accumulation effect also can be proved as in the following: Gd ion concentration will further accumulate at the tumor site, which can be found within a period of 20–48 h. Measurements of the accumulation effect of the nanocarrier in major organs and tumors of mice after the injection of UCNPs@BiOCl intravenously at different time points are shown in Fig. S10 (ESI†).

Conclusions

In summary, a novel UCNPs@BiOCl complex has been firstly designed and synthesized by integrating the BiOCl sheets with small UCNPs to achieve the 980 nm NIR light-induced PDT. UCNPs, which served as the energy converter, are modified with PAA, and BiOCl sheets are stabilized by the PEI, and then the two counterparts are integrated into the UCNPs@BiOCl complex *via* a condensation reaction of the amide. Upon 980 nm NIR light irradiation, the complex exhibits excellent antitumor efficiency for lots of ROS generation. Meanwhile, the introduction of UCNPs solved the question of tissue penetration for pure BiOCl sheets in the PDT treatment. Moreover, UCNPs also provide a support for image-guided tumor photodynamic therapy. In this way, our work may pave the way for the wide application of BiOCl-based materials in theranostics.

Experimental section

Materials and synthesis

All the reagents and chemicals were used as received in this experiment without any further purification, including Gd_2O_3, Yb_2O_3, nitric acid (HNO_3), cyclohexane, oleic acid (OA), and 1-octadecene (ODE), and Tm_2O_3 (from Sinopharm Chemical Reagent Co., Ltd, Shanghai, China), bismuth nitrate pentahydrate ($Bi(NO_3)_3{\cdot}5H_2O$), mannitol, sodium chloride (NaCl), polyethyleneimine (PEI, 25 kDa), poly acrylic acid (PAA, 1800 M_W), phosphate buffered saline (PBS), *N*-hydroxysuccinimide (NHS), 1-(3-dimethylaminopropyl)-3-ethylcarbodiimide hydrochloride (EDC), sodium hydroxide (NaOH), 4′,6-diamidino-2-phenylindole (DAPI), 1,3-diphenylisobenzofuran (DPBF), 3-4,5-dimethylthiazol-2-yl-2,5-diphenyl tetrazolium bromide (MTT), dimethyl sulfoxide (DMSO), calcein propidium iodide (PI) and AM (from Sigma-Aldrich).

Synthesis of BiOCl nanosheets

The BiOCl nanosheets were prepared according to the reported literature proposed by *Chen et al.*[43] Namely, 0.486 g of $Bi(NO_3)_3 \cdot 5H_2O$ and 0.455 g of mannitol were completely dispersed in 25 mL of deionized water with continuous ultrasonication. Subsequently, 5 mL of NaCl saturated solution was slowly injected into the mixture with stirring, and a uniform white suspension was formed. After stirring at room temperature for 30 min, the white suspension was transferred into a Teflon-lined stainless steel autoclave, which was heated at 160 °C for 3 h and then naturally cooled to room temperature. The resulting product was washed with deionized water several times and collected by centrifuge for the following experiment.

The BiOCl nanosheets were separately developed with ultrasonication for 30 min, and then added into excess amounts of PEI aqueous solution. After stirring for 24 h, the solution was further centrifuged with deionized water several times to remove the excessed PEI molecules.

Synthesis of OA-coated $NaGdF_4$:Yb,Tm@$NaGdF_4$

The OA-coated $NaGdF_4$:Yb,Tm@$NaGdF_4$ nanoparticles were prepared by a thermal-decomposition route. Mono-dispersed $NaGdF_4$:Yb,Tm were firstly obtained according to the following process: 1.0 mmol of $RE(OA)_3$ (RE = 79.5% Gd + 20% Yb + 0.5% Tm) and 12 mmol of NaF was added in a three-neck reaction vessel containing 15 mL of OA and 15 mL of ODE, and then gradually heated to 110 °C under a vacuum until free of bubbles to remove the water content and oxygen. After that, the mixture was heated to 310 °C, kept for 1.5 h under N_2 protection to yield a light-yellow uniform solution and cooled down to room temperature naturally. The $NaGdF_4$:Yb,Tm nanoparticles were collected by centrifugation, and alternately washed with ethanol and cyclohexane. Finally, the nanoparticles were dispersed in 5 mL of cyclohexane for later use. For the core–shell synthesis, the cyclohexane solution with $NaGdF_4$:Yb,Tm, 0.5 mmol of $Gd(CF_3COO)_3$ and 0.5 mmol of CF_3COONa were added in a three-neck reaction vessel containing 15 mL of OA and 15 mL of ODE, and subsequently heated at 120 °C under a vacuum until free of bubbles. After flushing with N_2, the solution was heated to 320 °C for 1.5 h to form a light-yellow solution before cooling down to room temperature naturally. The resulting nanoparticles was collected, washed with ethanol and cyclohexane and re-dispersed in 5 mL of cyclohexane. The core–shell up-conversion nanoparticles $NaGdF_4$:Yb,Tm@$NaGdF_4$ are denoted as UCNPs.

Synthesis of PAA–UCNPs

In brief, the carboxyl-functionalized PAA–UCNPs were obtained using a ligand exchange approach. 1 mmol of UCNPs in cyclohexane solution were poured into 20 mL of PAA aqueous solution containing 1 g of PAA, followed by 24 h of vigorous agitation. The obtained product was rinsed with deionized water and centrifuged to remove excessed PAA.

Synthesis of the UCNPs@BiOCl composite

Typically, as-prepared 1 mmol of PAA–UCNPs nanoparticles were dispersed in deionized water, then 3 mg of EDS and 6 mg of NHS were added to activate the carboxyl group of PAA. After the mixture was vigorously stirred for 2 h, certain amounts of the modified BiOCl nanosheets (PEI–BiOCl) and superfluous mPEG–NH_2 were added into the aforementioned PAA–UCNPs aqueous solution followed by 4 h agitation. The resulting UCNPs@BiOCl was washed with deionized water and collected by centrifugation.

Stability measurement

0.05 mg of UCNPs@BiOCl was incubated with normal saline (pH ~ 7.4), and fetal bovine serum at 37 °C under constant stirring. At designated time intervals, the solution of UCNPs@BiOCl was withdrawn and used for DLS and zeta potential measurements.

ROS detection

In this work, DPBF served as the ROS probe. 10 mg of the UCNPs@BiOCl complex was added into 2 mL of DPBF stock solution (0.5 mg mL^{-1}), and the mixture was kept in the dark. After ultrasonic treatment, it was exposed to 980 nm laser for specific time intervals (5 min, 10 min, 15 min, and 20 min) with an injected atmosphere. After centrifugation, the absorbance of the supernatant at 410 nm was monitored using a UV-vis spectrophotometer. In a contrast experiment, the absorbance of DPBF was recorded at 0 h, 12 h, and 24 h, respectively. The syntheses of $NaGdF_4$:Yb,Tm@$NaGdF_4$@black phosphorus (UCNPs@BPs) and $NaGdF_4$:Yb,Tm@$NaGdF_4$@TiO_2 (UCNPs@TiO_2) are based on previous reports.[71,72]

NIR laser-induced *in vitro* PDT performance

The NIR Laser-induced *in vitro* PDT performance by HeLa cancer cells (human cervical carcinoma cell line) was studied using CLSM. Briefly, the cells (~5×10^4 $well^{-1}$) were injected into six-well plates with coverslips and cultured in 5% CO_2 at 37 °C to form a monolayer. Subsequently, 2 mL per well of UCNPs@BiOCl (1 mg mL^{-1}) were placed into six-well plates for another 4 h culture and exposed to 980 nm laser (0.5 W cm^{-2}) for 10 min. To remove the residual material, the cells were washed three times with PBS, followed by staining with DCFH-DA for 20 min. After a further rinse with PBS, the results were monitored by CLSM. Simultaneously, the ROS detection process of BiOCl sheets was similar to that above. The only difference is exposure to UV light.

In vitro cell viability

The MTT assay was employed to detect the cytotoxicity of the UCNPs@BiOCl complex to L929 fibroblast cells. Firstly, the cells were placed into a 96-well plate with a density of around 7500 cells per well at 37 °C in a humidified incubator with 5% CO_2 for 24 h to form a monolayer. 0.1 mL of culture medium containing different concentrations of UCNPs@BiOCl (7.8, 15.6, 31.3, 62.5, 125, 250, and 500 μg mL^{-1}) were added into each well and cultured for another 24 h. Next, 0.02 mL per well of MTT stock solution (5 mg mL^{-1}) was placed into the plates and sequentially cultured for 4 h (5% CO_2, 37 °C). Finally, the suspension was replaced by 0.15 mL per well of DMSO. The mechanism of the MTT assay is that MTT can be reduced by

cytochrome *c* to produce water insoluble formazan in the metabolism of living cells. So, the amount of living cells is directly proportional to the absorbance at 488 nm of formazan. To help the formazan completely dissolve in DMSO solvent, the plate was shaken for 5 min. The data recorded using a micro-plate reader in this test was average calculated by the three parallel groups of each concentration.

Hemolysis assay

The human blood stabilized by EDTA.K2 was washed with PBS several times and centrifuged to collect the blood cells (RBCs). The red blood cells (RBCs) were obtained with a transparent supernatant solution appeared, followed by dilution to 1 : 10 with a PBS solution. Then, 1.2 mL of deionized water was mixed with 0.3 mL of diluted RBCs, which served as a positive control. The negative control group was replaced by 1.2 mL of PBS mixed with 0.3 mL of diluted RBCs. 1.2 mL of PBS solution containing different concentrations of UCNPs@BiOCl (7.8, 15.6, 31.3, 62.5, 125, 250, and 500 μg mL^{-1}) was mixed with 0.3 mL of diluted RBCs for the experimental group. Subsequently, the tubes were shaken and stood for 2 h. The absorbances at 541 nm of the upper supernatants were detected using UV/vis spectroscopy after centrifugation.

In vitro cytotoxicity

The detection process of the cytotoxicity test to cancer cells can also be borrowed from the MTT assay in the biocompatibility to L929 fibroblast cells. L929 fibroblast cells were replaced with HeLa cancer cells cultivated with a cell-culture medium, only 980 nm, and various concentrations of UCNPs@BiOCl complex with or without NIR light irradiation. Besides, the group treated with the culture medium served as a control blank group. The data were recorded using micro-plate reader and average calculated by three parallel groups of each concentration.

The detection process of the photodynamic effects has a strong resemblance to that of the dye experiment *in vitro* but the live and dead cells were stained with calcein AM (2 mM) and propidium iodide (PI, 5 mM) for 1 h.

Up-conversion luminescence microscopy (UCLM) observation

In brief, HeLa cells at a density of 5×10^4 $well^{-1}$ were placed into 6-well culture plates with a glass slide and cultured to form a monolayer at 37 °C in a humidified incubator with 5% CO_2 for 24 h. Subsequently, the culture medium was replaced by 2 mL of the as-prepared UCNPs@BiOCl (0.5 mg mL^{-1}) for 3 h. After washing steps by PBS twice at the indicated time points, the cells was fixed with 1 mL per well formaldehyde (2.5%) at 37 °C for 10 min and rinsed three times with PBS again. Finally, the cells were collected before monitoring by up-conversion luminescence microscopy.

In vivo anticancer therapy

The criteria of The National Regulation of China for Care and Use of Laboratory Animals for the processing on Female Balb/c (25–30 g) mice were complied with in all the experiments. The mice were provided by the Harbin Veterinary Research Institute of the Chinese Academy of Agricultural Sciences (Harbin, China). Typically, mice were subcutaneously injected with U14 cells (murine cervical carcinoma cell lines) into the left sub-axilla to produce the tumors, and they were partitioned into four groups randomly. After the tumor feature was approximately of bean size, the mice were treated under different conditions, including normal saline, pure 980 nm laser irradiation, pure UCNPs@BiOCl complex, and UCNPs@BiOCl complex with 980 nm laser irradiation. 0.1 mL of the tested materials (1 mg mL^{-1}) was injected and travels through the vein once in two days, and the tumor site exposed with NIR light at a pump power of 0.5 W cm^{-2} for 10 min after intravenous injection for 24 h. Traditionally, a control black group is replaced by the group treated with normal saline in this test and the tumor volumes and body weights of each mouse were recorded every two days. After the tumor-bearing mice were sacrificed at 14 days, the blood was collected for blood biochemistry and hematology analysis, and the tumor tissues and typical organs (kidney, lung, spleen, heart, and liver) were dissected for further histology analysis.

Measurement of the blood half time and accumulation effect in the tumor

Female tumor-bearing Balb/c mice were divided into six groups (five mice in each group) and injected with UCNPs@BiOCl nanoparticles (21 mg Gd kg^{-1}) intravenously. Then the mice blood and tissues were collected and treated with H_2O_2 and HNO_3 (volume ratio was 2 : 1) at 1, 3, 5, 12, 24 and 48 h after injection. ICP-MS was used for detecting the gadolinium element concentration in these solutions.

Characterization

Transmission electron microscopy (TEM) images were captured on a FEI Tecnai G^2 S-Twin with a field emission gun operating at 200 kV. X-ray powder diffraction (XRD) was recorded on a Rigaku D/max-TTR-III diffractometer using Cu-Kα radiation (λ = 0.15405 nm). A VG ESCALAB MK II electron energy spectrometer using Mg KR (1253.6 eV) was employed to measure the X-ray photoelectron spectrum (XPS). Atomic force microscopy (AFM) images were carried out on a CSPM5500. UCL emission spectra were obtained on Edinburgh FLS 980 using a 980 nm laser diode controller as separate laser sources. All the UC spectra in our experiment were gained under the same conditions with the same signal amplification. Fourier transform infrared spectroscopy (FT-IR) spectra were detected on a Perkin-Elmer 580B IR spectrophotometer using the KBr pellet as the background. Confocal laser scanning microscopy (CLSM) images were recorded using a Leica SP8. A UV-1601 spectrophotometer was used to characterize the UV-vis spectra of the samples in the wavelength range of 200 to 900 nm.

Acknowledgements

Financial support from the National Natural Science Foundation of China (NSFC 21401032, 51472058, 51332008), the Outstanding Youth Foundation of Heilongjiang Province (JC2015003), a

Heilongjiang Postdoctoral Special Fund (LBH-TZ0607) and a Special Financial Grant from the China Postdoctoral Science Foundation (2015T80321) and Fundamental Research Funds for the Central Universities of China are greatly acknowledged.

Notes and references

1 S. Lu, D. T. Tu, P. Hu, J. Xu, R. F. Li, M. Wang, Z. Chen, M. D. Huang and X. Y. Chen, *Angew. Chem., Int. Ed.*, 2015, **54**, 7915–7919.
2 Y. Chen, C. Tan, H. Zhang and L. Wang, *Chem. Soc. Rev.*, 2015, **44**, 2681–2701.
3 S. Gai, C. Li, P. Yang and J. Lin, *Chem. Rev.*, 2014, **114**, 2343–2389.
4 Y. Wang, H. Wang, D. Liu, S. Song, X. Wang and H. Zhang, *Biomaterials*, 2013, **34**, 7715–7724.
5 A. Punjabi, X. Wu, A. Tokatli-Apollon, M. El-Rifai, H. Lee, Y. Zhang, C. Wang, Z. Liu, E. M. Chan, C. Duan and G. Han, *ACS Nano*, 2014, **8**, 10621–10630.
6 H. Wan, Y. Zhang, W. B. Zhang and H. F. Zou, *ACS Appl. Mater. Interfaces*, 2015, **7**, 9608–9618.
7 P. Huang, J. Lin, X. S. Wang, Z. Wang, C. L. Zhang, M. He, K. Wang, F. Chen, Z. M. Li, G. X. Shen, D. X. Cui and X. Y. Chen, *Adv. Mater.*, 2012, **24**, 5104–5110.
8 Z. Li, C. Wang, L. Cheng, H. Gong, S. Yin, Q. Gong, Y. Li and Z. Liu, *Biomaterials*, 2013, **34**, 9160–9170.
9 L. M. Pan, J. A. Liu and J. L. Shi, *Adv. Funct. Mater.*, 2014, **24**, 7318–7327.
10 N. M. Idris, M. K. Gnanasammandhan, J. Zhang, P. C. Ho, R. Mahendran and Y. Zhang, *Nat. Med.*, 2012, **18**, 1580–U190.
11 Z. Kang, X. Yan, L. Zhao, Q. Liao, K. Zhao, H. Du, X. Zhang, X. Zhang and Y. Zhang, *Nano Res.*, 2015, **8**, 2004–2014.
12 C. Zhang, K. Zhao, W. Bu, D. Ni, Y. Liu, J. Feng and J. Shi, *Angew. Chem., Int. Ed.*, 2015, **54**, 1770–1774.
13 S. Zhang, D. Yang, D. Jing, H. Liu, L. Liu, Y. Jia, M. Gao, L. Guo and Z. Huo, *Nano Res.*, 2014, **7**, 1659–1669.
14 Z. Hou, Y. Zhang, K. Deng, Y. Chen, X. Li, X. Deng, Z. Cheng, H. Lian, C. Li and J. Lin, *ACS Nano*, 2015, **9**, 2584–2599.
15 L. Li, J. Yan, T. Wang, Z.-J. Zhao, J. Zhang, J. Gong and N. Guan, *Nat. Commun.*, 2015, **6**, 5881.
16 H. Zhang, R. Shi, A. Xie, J. Li, L. Chen, P. Chen, S. Li, F. Huang and Y. Shen, *ACS Appl. Mater. Interfaces*, 2013, **5**, 12317–12322.
17 J. Mou, T. Lin, F. Huang, H. Chen and J. Shi, *Biomaterials*, 2016, **84**, 13–24.
18 Y. Liu, Q. Yao, X. Wu, T. Chen, Y. Ma, C. N. Ong and J. Xie, *Nanoscale*, 2016, **8**, 10145–10151.
19 H. Li, X. He, Z. Kang, H. Huang, Y. Liu, J. Liu, S. Lian, C. H. A. Tsang, X. Yang and S.-T. Lee, *Angew. Chem., Int. Ed.*, 2010, **49**, 4430–4434.
20 L. S. Lin, Z. X. Cong, J. Li, K. M. Ke, S. S. Guo, H. H. Yang and G. N. Chen, *J. Mater. Chem. B*, 2014, **2**, 1031–1037.
21 J. Liu, Y. Liu, N. Y. Liu, Y. Z. Han, X. Zhang, H. Huang, Y. Lifshitz, S. T. Lee, J. Zhong and Z. H. Kang, *Science*, 2015, **347**, 970–974.
22 C. F. Chan, Y. Zhou, H. Y. Guo, J. Y. Zhang, L. J. Jiang, W. Chen, K. K. Shiu, W. K. Wong and K. L. Wong, *ChemPlusChem*, 2016, **81**, 535–540.
23 R. Chen, J. F. Zhang, Y. Wang, X. F. Chen, J. A. Zapien and C. S. Lee, *Nanoscale*, 2015, **7**, 17299–17305.
24 S. S. Lucky, N. M. Idris, Z. Li, K. Huang, K. C. Soo and Y. Zhang, *ACS Nano*, 2015, **9**, 191–205.
25 L. Zeng, Y. Pan, Y. Tian, X. Wang, W. Ren, S. Wang, G. Lu and A. Wu, *Biomaterials*, 2015, **57**, 93–106.
26 L. Zeng, W. Ren, L. Xiang, J. Zheng, B. Chen and A. Wu, *Nanoscale*, 2013, **5**, 2107–2113.
27 C. Zhang, K. Zhao, W. Bu, D. Ni, Y. Liu, J. Feng and J. Shi, *Angew. Chem., Int. Ed.*, 2015, **54**, 1770–1774.
28 H. Zhang, B. Chen, H. Jiang, C. Wang, H. Wang and X. Wang, *Biomaterials*, 2011, **32**, 1906–1914.
29 Z. Hu, J. Li, C. Li, S. Zhao, N. Li, Y. Wang, F. Wei, L. Chen and Y. Huang, *J. Mater. Chem. B*, 2013, **1**, 5003–5013.
30 Z. Kang, X. Yan, L. Zhao, Q. Liao, K. Zhao, H. Du, X. Zhang, X. Zhang and Y. Zhang, *Nano Res.*, 2015, **8**, 2004–2014.
31 J. Li, D. Guo, X. Wang, H. Wang, H. Jiang and B. Chen, *Nanoscale Res. Lett.*, 2010, **5**, 1063–1071.
32 D. J. Martin, P. J. T. Reardon, S. J. A. Moniz and J. Tang, *J. Am. Chem. Soc.*, 2014, **136**, 12568–12571.
33 C. K. Chen, H. M. Chen, C.-J. Chen and R.-S. Liu, *Chem. Commun.*, 2013, **49**, 7917–7919.
34 I. S. Turan, D. Yildiz, A. Turksoy, G. Gunaydin and E. U. Akkaya, *Angew. Chem., Int. Ed.*, 2016, **55**, 2875–2878.
35 W. Zhu, Z. Dong, T. Fu, J. Liu, Q. Chen, Y. Li, R. Zhu, L. Xu and Z. Liu, *Adv. Funct. Mater.*, 2016, **26**, 5490–5498.
36 C. K. Chen, H. M. Chen, C. J. Chen and R. S. Liu, *Chem. Commun.*, 2013, **49**, 7917–7919.
37 H. Cheng, B. Huang and Y. Dai, *Nanoscale*, 2014, **6**, 2009–2026.
38 L. Ye, Y. Su, X. Jin, H. Xie and C. Zhang, *Environ. Sci.: Nano*, 2014, **1**, 90–112.
39 J. Li, Y. Yu and L. Zhang, *Nanoscale*, 2014, **6**, 8473–8488.
40 K. Zhao, L. Zhang, J. Wang, Q. Li, W. He and J. J. Yin, *J. Am. Chem. Soc.*, 2013, **135**, 15750–15753.
41 K.-L. Zhang, C.-M. Liu, F.-Q. Huang, C. Zheng and W.-D. Wang, *Appl. Catal., B*, 2006, **68**, 125–129.
42 Y. Xu, Z. Shi, L. E. Zhang, E. M. B. Brown and A. Wu, *Nanoscale*, 2016, **8**, 12715–12722.
43 J. Xiong, G. Cheng, G. Li, F. Qin and R. Chen, *RSC Adv.*, 2011, **1**, 1542–1553.
44 M. Guan, C. Xiao, J. Zhang, S. Fan, R. An, Q. Cheng, J. Xie, M. Zhou, B. Ye and Y. Xie, *J. Am. Chem. Soc.*, 2013, **135**, 10411–10417.
45 X. Zhang and L. Zhang, *J. Phys. Chem. C*, 2010, **114**, 18198–18206.
46 L. Ye, L. Zan, L. Tian, T. Peng and J. Zhang, *Chem. Commun.*, 2011, **47**, 6951–6953.
47 L. Ye, C. Gong, J. Liu, L. Tian, T. Peng, K. Deng and L. Zan, *J. Mater. Chem.*, 2012, **22**, 8354–8360.
48 L. Ye, J. Liu, C. Gong, L. Tian, T. Peng and L. Zan, *ACS Catal.*, 2012, **2**, 1677–1683.
49 L. Ye, J. Liu, Z. Jiang, T. Peng and L. Zan, *Appl. Catal., B*, 2013, **142**, 1–7.

50 L. Zhang, Z. Han, W. Wang, X. Li, Y. Su, D. Jiang, X. Lei and S. Sun, *Chem. – Eur. J.*, 2015, **21**, 18089–18094.
51 H. Wen, H. Zhu, X. Chen, T. F. Hung, B. Wang, G. Zhu, S. F. Yu and F. Wang, *Angew. Chem., Int. Ed.*, 2013, **52**, 13419–13423.
52 F. Wang, R. Deng, J. Wang, Q. Wang, Y. Han, H. Zhu, X. Chen and X. Liu, *Nat. Mater.*, 2011, **10**, 968–973.
53 F. Vetrone, R. Naccache, V. Mahalingam, C. G. Morgan and J. A. Capobianco, *Adv. Funct. Mater.*, 2009, **19**, 2924–2929.
54 Y. Zhong, G. Tian, Z. Gu, Y. Yang, L. Gu, Y. Zhao, Y. Ma and J. Yao, *Adv. Mater.*, 2014, **26**, 2831–2837.
55 X. Xie, N. Gao, R. Deng, Q. Sun, Q.-H. Xu and X. Liu, *J. Am. Chem. Soc.*, 2013, **135**, 12608–12611.
56 Q. Su, S. Han, X. Xie, H. Zhu, H. Chen, C.-K. Chen, R.-S. Liu, X. Chen, F. Wang and X. Liu, *J. Am. Chem. Soc.*, 2012, **134**, 20849–20857.
57 M. Guan, H. Dong, J. Ge, D. Chen, L. Sun, S. Li, C. Wang, C. Yan, P. Wang and C. Shu, *NPG Asia Mater.*, 2015, **7**, e205.
58 D. Yang, P. A. Ma, Z. Hou, Z. Cheng, C. Li and J. Lin, *Chem. Soc. Rev.*, 2015, **44**, 1416–1448.
59 L. Q. Xiong, T. S. Yang, Y. Yang, C. J. Xu and F. Y. Li, *Biomaterials*, 2010, **31**, 7078–7085.
60 F. Wang, D. Banerjee, Y. S. Liu, X. Y. Chen and X. G. Liu, *Analyst*, 2010, **135**, 1839–1854.
61 W. Li, J. Wang, J. Ren and X. Qu, *J. Am. Chem. Soc.*, 2014, **136**, 2248–2251.
62 S. Wu and H.-J. Butt, *Adv. Mater.*, 2016, **28**, 1208–1226.
63 F. Lu, L. Yang, Y. Ding and J.-J. Zhu, *Adv. Funct. Mater.*, 2016, **26**, 4778–4785.
64 S. Zeng, Z. Yi, W. Lu, C. Qian, H. Wang, L. Rao, T. Zeng, H. Liu, H. Liu, B. Fei and J. Hao, *Adv. Funct. Mater.*, 2014, **24**, 4051–4059.
65 K. Liu, X. Liu, Q. Zeng, Y. Zhang, L. Tu, T. Liu, X. Kong, Y. Wang, F. Cao, S. A. G. Lambrechts, M. C. G. Aalders and H. Zhang, *ACS Nano*, 2012, **6**, 4054–4062.
66 G. Chen, C. Yang and P. N. Prasad, *Acc. Chem. Res.*, 2013, **46**, 1474–1486.
67 Y. Min, J. Li, F. Liu, E. K. L. Yeow and B. Xing, *Angew. Chem., Int. Ed.*, 2014, **53**, 1012–1016.
68 L. D. Sun, Y. F. Wang and C. H. Yan, *Acc. Chem. Res.*, 2014, **47**, 1001–1009.
69 Y. Wang, S. Song, J. Liu, D. Liu and H. Zhang, *Angew. Chem., Int. Ed.*, 2015, **54**, 536–540.
70 H. Schaefer, P. Ptacek, O. Zerzouf and M. Haase, *Adv. Funct. Mater.*, 2008, **18**, 2913–2918.
71 C. Lv, D. Yang, P. Yang and J. Xu, *Chem. Mater.*, 2016, **28**, 4724–4734.
72 Z. Hou, Y. Zhang, K. Deng and Y. Chen, *ACS Nano*, 2015, **9**, 2584–2599.